

Statics Modeling of Discrete Joint Surgical Probes with Tendon-based Stiffening

Abstract—Minimally-invasive surgical (MIS) robots have the potential to reduce post-operative pain and complications, but must be able to follow tortuous paths to reach deep into the body. Our prior work on a MIS robot called the “highly articulated robot probe” (HARP) enabled follow-the-leader motion using two concentrically driven segmented tubes that alternate between locking and advancing each segment. By varying the tendon tension, such robots can be both steerable during insertion for deep unsupported access and become rigid to provide a stable platform for clinical intervention. To design and control such robots, a statics model is essential, but existing statics models do not meet the need to predict HARP’s payload capacity and required tendon tension for any arbitrary shape. This paper presents a 3D statics model that meets this need by introducing a mathematical formulation of the link-to-link friction effects as well as the external load conditions. This model provides a prediction of the maximum admissible external load for any given robot shape. We also investigate how the payload capacity is influenced not only by the robot’s shape, but also the actuation tendon forces, and validated the statics model experimentally on a prototype HARP platform. Our data demonstrates that the proposed model can predict the payload capacity with mean error of 0.15 N and max error of 0.64 N. The model presented in this paper will enable future design, control, and planning methods with HARP robots to optimize payload capacity for MIS tasks.

I. INTRODUCTION

The use of minimally invasive tools has the potential to reduce post-operative pain for patients. Naturally, we want these tools to be strong enough to exert the necessary forces on the anatomy, but soft enough so as to not cause collateral damage [1], [2]. Recent work in highly articulated robots, or so-called snake robots, have extended the reach of minimally invasive devices in that a physician can steer the robot deeper into the anatomy, reaching locations not necessarily within line of sight of the small surgical incision [3]. The problem is that the tortuous paths a highly articulated probe may follow could cause a loss of stiffness. This work develops a model for the statics of a particularly “highly articulated robot probe” (HARP), as shown in Fig. 1a. With this model in-hand, one can better design and control such a robot.

The HARP architecture consists of two concentric tendon-driven segmented snakes, the inner snake and outer snake, where each snake consists of a series of discrete rigid links [4]. By varying the actuation tendon tension of one snake and relying on the link-to-link friction, each snake can change from being steerable to being rigid. When the snake is steerable, the snake’s steering angle can be adjusted. By alternating the state

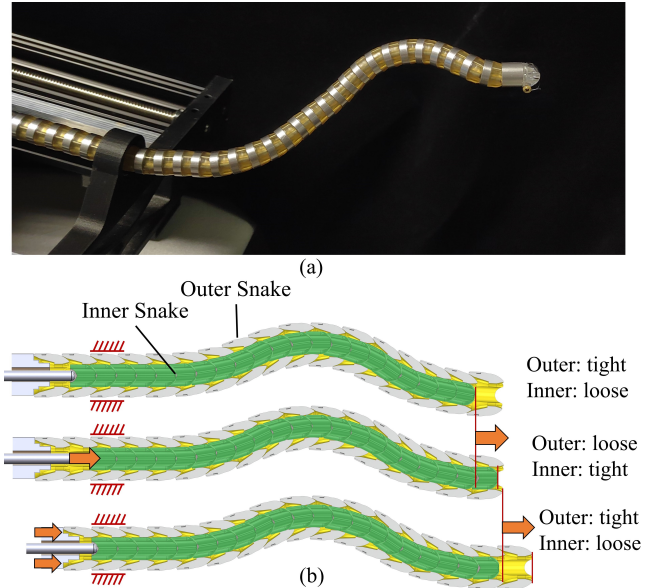


Fig. 1. The HARP. (a) A prototype of the HARP platform. (b) The “follow-the-leader” behavior achieved by alternating which snake is rigid/loose and advancing/steering the snakes in a step-wise fashion.

of each snake in an opposing step-wise fashion, a “follow-the-leader” behavior can be achieved as shown in Fig. 1b.

A variety of mechanical design architectures have been presented for surgical robots [5]–[7]. In the context of prior designs, the HARP system is tendon-actuated and discrete-jointed, similar to [8]–[10], and is related to [11] in its use of actuation tendon tension to adjust its stiffness/heading. HARP is unique in being both highly articulated and able to vary its stiffness while being under-actuated. HARP’s ability to follow arbitrary curves, unsupported, in 3D space can enable deeper surgical access. Further, its ability to vary its stiffness can allow it to navigate deep into the body while still having the payload capacity to manipulate tissue with lower deflections than a typical flexible continuum robot [5].

The combination of these features makes the HARP design architecture a favorable candidate for endoluminal/transluminal procedures where forceful manipulation is needed. For better robot control in such procedures, a statics model is essential to predict the HARP’s payload capacity and required tendon tension for any arbitrary shape. As reviewed in [5], [7], many prior works have presented statics models for various surgical manipulator architectures, including rigid-link devices [12], [13] and continuum devices [14]–[16]. However, none of these works address HARP’s need for a

3D statics model for the payload prediction. Such a statics model is also important because it would enable one to modulate the maximum force direction online by varying the actuation tendon tensions, and to plan paths within the body to maximize payload. The required actuation forces in the straight configuration were provided in [4]. In [17], a model for a robot similar to HARP was presented, but the validation was limited to a single configuration and the payload capacity was not considered for any arbitrary shape.

As a step towards addressing these limitations of prior work, this paper presents a 3D statics model for one tendon-actuated snake (the outer snake) of HARP. HARP has both an inner snake and an outer snake, but we focus on the outer snake because its three actuation tendons and larger radius provide a higher payload than the inner snake. Typically, once in position, both the inner and outer snakes would be locked. By only considering the outer snake, we present a conservative estimate which provides the majority of HARP's payload capacity once the target surgical site is reached. Our proposed model includes the effect of link geometry, link-to-link friction, actuation tendon forces, and external forces applied to the robot. We show how the model can be used to 1) predict the maximum admissible external load for any shape and 2) predict the change in maximum payload when the actuation tendon tension or the snake shape changes. Finally, we experimentally validate the statics model and demonstrate the ability to modulate the payload capacity by varying the individual actuation tendon tensions.

II. STATICS MODEL FORMULATION

In this section, we present a statics model for the outer segment of HARP, including the effect of link-to-link friction and external loading.

A. Robot Kinematics

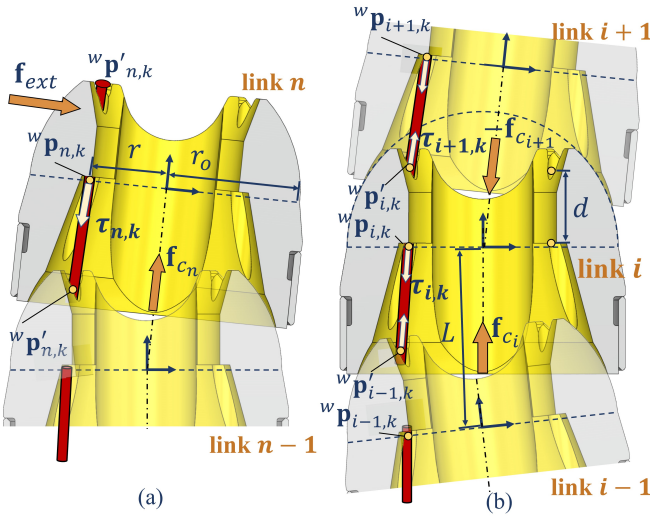


Fig. 2. Kinematics diagram for the HARP outer segment. (a) Distal links in the front of the snake robot. (b) Middle link i and its two adjacent links along the body of the snake robot.

We assume the robot has n links that there are three tendon channels 120° apart axially. The kinematic representation of two adjacent links is shown in Fig. 2a. We define the body frame of any link i as a frame attached to the link's geometric center. The k^{th} tendon ($k = 1, 2, 3$) passes into and out of the channel of link i at the points ${}^b\mathbf{p}_{i,k}$ and ${}^b\mathbf{p}'_{i,k}$, respectively. These two points are expressed in the body frame of link i :

$${}^b\mathbf{p}_{i,k} = \left[0, r \sin\left(\frac{2(k-1)}{3}\pi\right), r \cos\left(\frac{2(k-1)}{3}\pi\right) \right]^T \quad (1)$$

$${}^b\mathbf{p}'_{i,k} = \mathbf{p}_{i,k} + [d, 0, 0]^T \quad (2)$$

where k is the index of the tendon number, r is the distance from the center of the tendon channel to the link center, and d is the length of the link channel.

Following [18], the relative rotation between link $i-1$ and link i is represented by the bending angle ϕ_i and the directional angle θ_i . This provides the homogeneous transformation matrix between the two links:

$${}^{i-1}\mathbf{T}_i = \begin{bmatrix} {}^{i-1}\mathbf{R}_i & {}^{i-1}\mathbf{t}_i \\ \mathbf{0} & 1 \end{bmatrix} \in SE(3) \quad (3)$$

$${}^{i-1}\mathbf{R}_i = \mathbf{R}_x(\theta_i) \mathbf{R}_y(\phi_i) \mathbf{R}_x(-\theta_i) \in SO(3) \quad (4)$$

$${}^{i-1}\mathbf{t}_i = {}^{i-1}\mathbf{R}_i [L \ 0 \ 0]^T \in \mathbb{R}^3$$

The matrix \mathbf{R}_x and \mathbf{R}_y are the rotation matrices that rotate a 3-D vector about the x -axis and y -axis, respectively, and L is the length of each link. The homogeneous transformation matrix between any two links' body frames is given by:

$${}^m\mathbf{T}_i = \prod_{j=m+1}^i {}^{j-1}\mathbf{T}_j \in SE(3) \quad (5)$$

We use ${}^m\mathbf{T}_i$ to transform the vertices where the tendons pass into and out of the link's channel into any frame m , i.e.. ${}^m\bar{\mathbf{p}}_{i,k} = {}^m\mathbf{T}_i {}^b\bar{\mathbf{p}}_{i,k}$ and ${}^m\bar{\mathbf{p}}'_{i,k} = {}^m\mathbf{T}_i {}^b\bar{\mathbf{p}}'_{i,k}$. where $\bar{\mathbf{a}} = [\mathbf{a} \ 1]^T$.

B. Static Model

We now consider the forces and moments applied to a single link. For the distal link n (Fig. 2a), the forces applied to the link include the actuation tendon tensions, the external force applied to the link, the contact force from link $n-1$, and the gravity force. The actuation tendon tensions are given by:

$$\tau_{n,k} = T_k \frac{{}^w\mathbf{p}_{n,k} - {}^w\mathbf{p}'_{n-1,k}}{\|{}^w\mathbf{p}_{n,k} - {}^w\mathbf{p}'_{n-1,k}\|} \in \mathbb{R}^3 \quad (6)$$

where T_k is the tension on the k tendon, and ${}^w\mathbf{p}_{n,k}$ and ${}^w\mathbf{p}_{n,k}$ are the vertices of the tendon channel expressed in the world frame (attached to the center of the base link). Here we assume the actuation tendon tension keeps constant along the link channels. The external force is defined as $\mathbf{f}_{ext} = F_{ext}\hat{\mathbf{n}}_{ext}$, where F_{ext} is the magnitude of the external force and $\hat{\mathbf{n}}_{ext}$ is the unit vector defining the external force direction. The contact force from link $n-1$ is given by $\mathbf{f}_{cn} = F_{cn}\hat{\mathbf{n}}_{cn}$, where F_{cn} is the magnitude and $\hat{\mathbf{n}}_{cn}$ is the unit vector defining the contact force direction. Finally, the gravity force is similarly

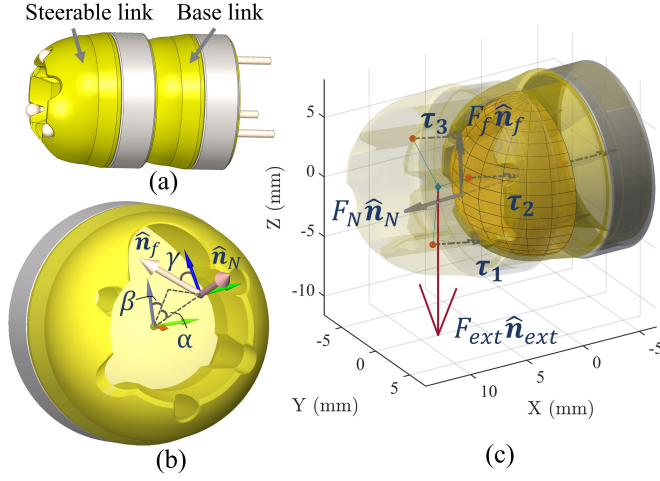


Fig. 3. The static force diagram for a two-link system. (a) Two-link system. (b) The direction of the normal reaction force and friction force between the two-link surfaces. (c) All forces applied to the steerable link.

given by $\mathbf{f}_{g_n} = F_{g_n} \hat{\mathbf{n}}_g$, where F_g is the magnitude and $\hat{\mathbf{n}}_g$ is the unit direction. For this two-link formulation, we assume the external force is applied on the center point of the distal link frame. We note that these forces are also defined in the world frame. We then have the force equilibrium equations of the distal link as:

$$\sum_{k=1}^3 \tau_{n,k} + \mathbf{f}_{c_n} + \mathbf{f}_{ext} + \mathbf{f}_{g_n} = \mathbf{0} \quad (7)$$

For a middle link, shown in Fig. 2b, there are additional forces applied to the link. These include the contact force from the previous link and the actuation tendon forces from the two adjacent links. The forces from the actuation tendons are given by:

$$\begin{aligned} \tau_{i,k}^{\text{net}} &= \tau_{i,k} - \tau_{i+1,k} \\ &= T_k \frac{{}^w \mathbf{p}_{i,k} - {}^w \mathbf{p}'_{i-1,k}}{\| {}^w \mathbf{p}_{i,k} - {}^w \mathbf{p}'_{i-1,k} \|} + T_k \frac{{}^w \mathbf{p}'_{i,k} - {}^w \mathbf{p}_{i+1,k}}{\| {}^w \mathbf{p}'_{i,k} - {}^w \mathbf{p}_{i+1,k} \|} \end{aligned} \quad (8)$$

The force equilibrium equations for the middle link i are therefore:

$$\sum_{k=1}^3 \tau_{i,k}^{\text{net}} + \mathbf{f}_{c_i} - \mathbf{f}_{c_{i+1}} + \sum_{k=1}^n \mathbf{f}_{g_k} = \mathbf{0} \quad (9)$$

By listing the force equilibrium equations (7) and (9) from link i to n , we can show through cancellation of contact force and actuation tendon terms that the force equilibrium for any link i is:

$$\sum_{k=1}^3 \tau_{i,k} + \mathbf{f}_{ext} + \mathbf{f}_{c_i} + \sum_{k=1}^n \mathbf{f}_{g_k} = \mathbf{0} \quad (10)$$

We now formulate the contact force \mathbf{f}_{c_i} between two links, where a steerable link, driven by three tendons and pushed by an external load, is held to a fixed base link, as shown in Fig. 3(a). We model the two links as a ball and socket and following the modeling work on spherical joints [19], [20], we simplify the assumption that the contact between the two spherical surfaces is a single point contact where the contact

point on the spherical surface can change, depending on the steering angle and the direction of external load. Adopting the Coulomb static friction model, each contact force consists of a normal reaction force and a perpendicular friction force. With a larger contact force, a higher friction moment will resist the rotation between the contact surfaces, stiffening the links.

In the base link frame, as shown in Fig. 3(b), the direction of the normal reaction force is defined by a unit vector $\hat{\mathbf{n}}_N = [\sin \alpha, \cos \alpha \sin \beta, \cos \alpha \cos \beta]^T$, where α is the angle between $\hat{\mathbf{n}}_N$ and the $y-z$ plane, β is the angle between $\hat{\mathbf{n}}_N$ and the z -axis projected to the $y-z$ plane. These variables also allow us to define a contact frame whose origin is at the contact point and whose x -axis is aligned with $\hat{\mathbf{n}}_{N_i}$:

$${}^b \mathbf{T}_{c_i} = \begin{bmatrix} {}^b \mathbf{R}_{c_i} & {}^b \mathbf{R}_{c_i} [r_o, 0, 0]^T \\ \mathbf{0} & 1 \end{bmatrix} \quad (11)$$

where ${}^b \mathbf{R}_{c_i} = \mathbf{R}_x(-\beta) \mathbf{R}_y(\alpha - \frac{\pi}{2})$. The unit vector defining the direction of the friction force is perpendicular to $\hat{\mathbf{n}}_{N_i}$ and is given by:

$$\hat{\mathbf{n}}_{f_i} = {}^b \mathbf{R}_{c_i} [0, -\cos \gamma, \sin \gamma]^T \quad (12)$$

where γ indicates the angle between $\hat{\mathbf{n}}_f$ and the contact frame's z -axis direction of friction in the contact frame, as shown in Fig. 3(b). The contact force finally is given by:

$$\mathbf{f}_{c_i} = F_{N_i} \hat{\mathbf{n}}_{N_i} + F_{f_i} \hat{\mathbf{n}}_{f_i} \quad (13)$$

where F_{N_i} and F_{f_i} are the magnitude of the normal reaction force and friction force, respectively. Following [20], we use (13) together with $F_{f_i} = \mu F_{N_i}$, to derive the magnitude of the friction force:

$$F_{f_i} = \frac{\mu F_{c_i}}{\sqrt{1 + \mu^2}} \quad (14)$$

which also provides the magnitude of the normal force via $F_{f_i} = \mu F_{N_i}$.

To complete the statics model, the moment equilibrium equations are also required. Since the steerable link rotates around the base link's spherical surface, the normal reaction force will pass through the base link's center. Following the same steps as with the force equilibrium, the moment equilibrium for the steerable link about its rotation center can be derived as:

$$\sum_{k=1}^3 \mathbf{r}_{k_i} \times \tau_{i,k} + \mathbf{m}_{ext} + \mathbf{m}_{f_i} + \mathbf{m}_{g_i} = \mathbf{0} \quad (15)$$

In this equation, $\mathbf{m}_{ext} = \mathbf{r}_{ext} \times F_{ext} \hat{\mathbf{n}}_{ext}$ is the moment due to the external force, where \mathbf{r}_{ext} is a vector from the base link frame origin to the location at which the external force is applied. The moment due to the contact point friction is denoted by $\mathbf{m}_{f_i} = r_o \hat{\mathbf{n}}_{N_i} \times F_{f_i} \hat{\mathbf{n}}_{f_i}$, where r_o is the radius of the outer link, and the moment due to gravity is given by $\mathbf{m}_{g_i} = \mathbf{r}_i \times F_{g_i} \hat{\mathbf{n}}_{g_i}$.

To determine the load at which the link will slip, we consider both the force equilibrium equation and the moment equilibrium equation. Given a set of tendon tensions τ_k , we do this by first solving for the values of F_{ext} , α , β and γ that

satisfy the force equilibrium (10), assuming that $F_{f_i} = \mu F_{N_i}$ (i.e. the condition for slip). We then solve for the same variables that satisfy the moment equilibrium, once again assuming that $F_{f_i} = \mu F_{N_i}$. We then take the lower value of F_{ext} as the payload capacity of the link. Additional details on the numerical approach to solving these problems are given below.

To extend to a multi-link system, we use a similar model as with the two-link system, but we write the force and moment equilibrium equations in the body frame of link $i - 1$, which preserves the definition of the contact force as shown in Fig. 3. This will result in the force and moment equilibrium equations similar to (10) and (15). We can then determine the payload capacity for each link in the snake. To determine the payload capacity for the entire snake, we take the minimum payload capacity across all links. With this approach, we also determine the “weakest link” in the robot, i.e the link which will fail first.

C. Numerical Solution

As described above, we solve for the payload by numerically solving for the values of F_{ext} , α , β and γ that satisfy the force equilibrium (10). We then repeat this for the moment equilibrium, and take the minimum value of F_{ext} between them as the payload capacity for the link. We solve these systems of equations using an interior point constrained nonlinear minimization solver via *fmincon()* in MATLAB.

We note that multiple solutions can exist. As an example, the same force balance equations can be satisfied with one contact force that is physically on the link sphere and a second where the contact force is in the opposite side of the sphere (but is not physically on the sphere) and in the opposite direction. To help address this, we add additional constraints to ensure physically feasible directions and magnitudes for the contact force. The first constraints is that the magnitude of the external force is positive, i.e. $F_{ext} > 0$. The second set of constraints ensure that the contact force is physically on the surface of the sphere: $20^\circ < \alpha < 90^\circ$, $-180^\circ < \beta < 180^\circ$, and $-180^\circ < \gamma < 180^\circ$. For each link, we furthermore ran the solver with three different initial guesses, and took the result with the lowest residual error among the three. Using this approach, computing the payload for the two-link system takes roughly 0.18 seconds on a desktop PC with a i7-11700 2.50 GHz CPU.

The two-link payload capacity is then used to predict the maximum external force the entire outer snake can support. We first define the external force direction and the action point, and then transform the external force into the body frame of each link $i - 1$. We then solve for the maximum payload for each two-link statics models by iterating through every link from the distal link to the base link. We take the smallest payload capacity among all links as the payload capacity of the robot. This also defines the weakest link of the robot, which is the link that will be the first to slip when the external load is increased to the maximum payload from zero.

III. DETERMINING THE PAYLOAD CONE

This section presents how this proposed statics model can be used to analyze the payload capacity of the HARP robot. We consider the payload capacity as the maximum external force that can be exerted on the robot without causing a slip between any two links, which represents the maximum force that a surgeon can apply to tissue.

The statics model shown in the previous section assumes the external force direction is known, however, in practice, it can be difficult to know *a priori* the exact direction of forces that a surgical task may require. For this reason, in this section, we define a *payload cone* that allows us to examine the maximum permissible forces (payload) in all possible directions. As we will show below, this allows us to determine the minimum external force magnitude that the overall robot can support for all possible external loads .

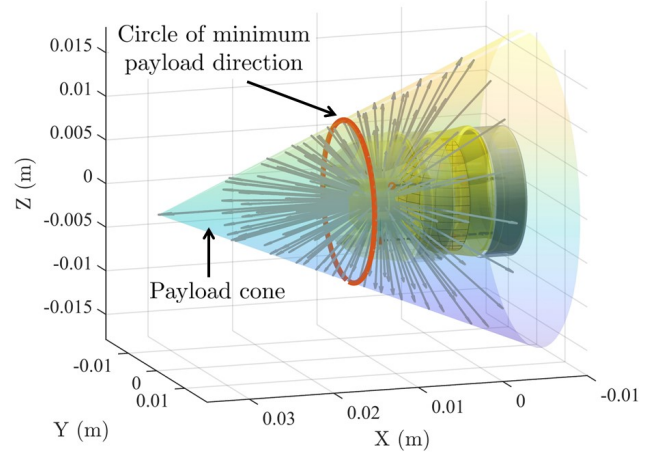


Fig. 4. The payload cone for a two-link system. the payload cone is formed by an envelope of payloads in different directions (grey arrows), and the red circle shows the directions of minimum payload capacity. The length of each arrow indicates the payload magnitude.

We define the payload direction as $\hat{\mathbf{n}}_p = [\cos \theta_p, \sin \theta_p \sin \phi_p, -\sin \theta_p \cos \phi_p]$, where θ_p is the angle between $\hat{\mathbf{n}}_p$ and the base link's x -axis and ϕ_p is the angle between $\hat{\mathbf{n}}_p$ and the y -axis after projecting $\hat{\mathbf{n}}_p$ to $y - z$ plane. Fig. 4 shows the payload cone. The payload directions are indicated by the grey arrows, which represents the magnitude of the payload capacity using arrow length. It is found that all the arrows are enveloped by a cone, which can be seen by substituting (13) into (10) and rewriting as:

$$\mathbf{f}_{ext} = - \sum_{k=1}^3 \boldsymbol{\tau}_{i,k} - (F_{N_i} \hat{\mathbf{n}}_{N_i} + F_{f_i} \hat{\mathbf{n}}_{f_i}) \quad (16)$$

where we have dropped the gravity for brevity. From the Coulomb friction model, it is known that $\mathbf{f}_{c_i} \leq (F_{N_i} \hat{\mathbf{n}}_{N_i} + \mu F_{N_i} \hat{\mathbf{n}}_{f_i})$ defines a friction cone for a point contact. The actuation tensions in $\sum_{k=1}^3 \boldsymbol{\tau}_{i,k}$ in (16) then shift the orientation and the position of this friction cone, resulting in the robot's *payload cone*.

In the straight configuration, the payload cone has infinite height, since (setting aside the problem of buckling) the tip of the robot can support infinitely high forces along its longitudinal axis. For visualization purposes, Fig. 4 therefore only shows the payloads with $\theta_p < 135^\circ$.

We argue that the size of the payload cone indicates the overall payload capacity of the probe in a particular configuration. The cone's size is determined by the cone's apex angle, which in turn, is determined by the payload capacity in the direction of minimum payload. Fig. 4 shows the circle of directions of the payloads with the minimum magnitude for a two-link system. It is found by solving the statics model above, but with an additional constraint:

$$\hat{\mathbf{n}}_p \cdot (F_{N_i} \hat{\mathbf{n}}_{N_i} + F_{f_i} \hat{\mathbf{n}}_f) = 0 \quad (17)$$

This constraint ensures that the payload direction is perpendicular to the contact force, which is the direction in which the lowest force is needed to cause slip.

We have presented the definition of the payload cone here to demonstrate the utility of our model in scenarios where the direction of the external load is not known. Whether the external force is measured or not, we can still use our statics model, together with the definition of the payload cone, to determine the minimum payload capacity for a given snake configuration.

IV. EXPERIMENTAL MODEL VALIDATION

In this section, the proposed statics model is validated with payload experiments on a prototype HARP robot.

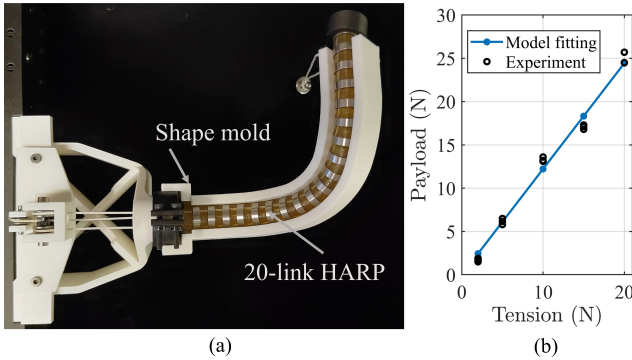


Fig. 5. Experiment setup and friction coefficient calibration. (a) Payload testing setup on a 20-link HARP robot. (b) Friction coefficient calibration results using a two-link system. (Sample number N=3)

A. Experiment Setup and Friction Coefficient Calibration

Fig. 5a shows the experiment setup of the payload testing. Our HARP robot has three actuation tendons controlling the outer snake, which has 20 links with a total length of 170 mm and an outer diameter of 12.7 mm. The kinematic radius of the actuation tendons is 4.95 mm. A 3D-printed mold is used to set the ground-truth robot configuration. The tendon tensions are maintained by hanging known weights on each tendon. After removing the mold, we incrementally increased the force applied to the snake's tip by hanging known weights to the tip. We observed that the link slip happened suddenly when

the applied force reached a certain value. For each test, we recorded the weight that caused the robot to slip, and compared this experimentally determined payload capacity to our model prediction.

We used a similar process (but using only two links) to calibrate the friction coefficient before we validated the full model. The static model is fitted to the experiment data using a least-squares fitting, with the results shown in Fig. 5b. The calibrated friction coefficient was 0.58, which is similar to the nominally estimated friction coefficient of 0.5 [4].

B. Experimental Validation with Equal Tensions

The proposed statics model was verified on the four different snake shapes shown in Fig. 6: straight, horizontal S-shape, vertical S-shape, and a non-planar spatial shapes. The three actuation tendons were set to the same tension, ranging from 5 N to 35 N at intervals of 5 N. We applied incrementally larger loads to the tip of the snake, and after the snake slipped, we recorded the applied weight, reset the snake shape using the 3D printed mold, and reran the experiment. This was done five times for each set of applied tension loads. We then compared these experimentally determined payload capacities to our models' prediction.

As shown in Fig. 6, the payload capacity increases linearly with the actuation tension, matching what our model predicted. The mean payload capacity errors and the maximum payload capacity errors are given in Table I. Over all experiments, our model predicted the payload capacity with a mean error of 0.15 N and a maximum error below 0.64 N. As shown in Fig. 6, the experimentally determined payload could vary as much as 0.5 N for a single set of actuation tendon loads, so we believe our reported maximum error is reasonable to validate the proposed model.

TABLE I
EXPERIMENTAL ERROR OF PAYLOAD CAPACITY

Shape	Mean Error	Max Error
Straight	0.07 N (6.05%)	0.11 N (8.30%)
Vertical S-shape	0.06 N (4.29%)	0.11 N (7.56%)
Horizontal S-shape	0.10 N (10.69%)	0.16 N (32%)
Non-planar Spatial Shape	0.37 N (22.3%)	0.64 N (39.9%)

The largest errors occurred with the non-planar curved shape. A potential explanation for this larger error is the additional difficulty for the non-planar shape in ensuring that all links are aligned when manually placing the snake into the 3D-printed mold. The effects of unmodeled friction loss in the actuation tendons, which our model does not account for, may also play a larger role in the non-planar spatial shape due to its higher curvature.

C. Experimental Validation with Non-equal Tension

Payload testings were also conducted by setting different tensions to the actuation tendons. We observed that by setting the tension T_1 to be 5 N less than the other two tendons, the payload capacity can increase by up to 35.50% and 24.51% for

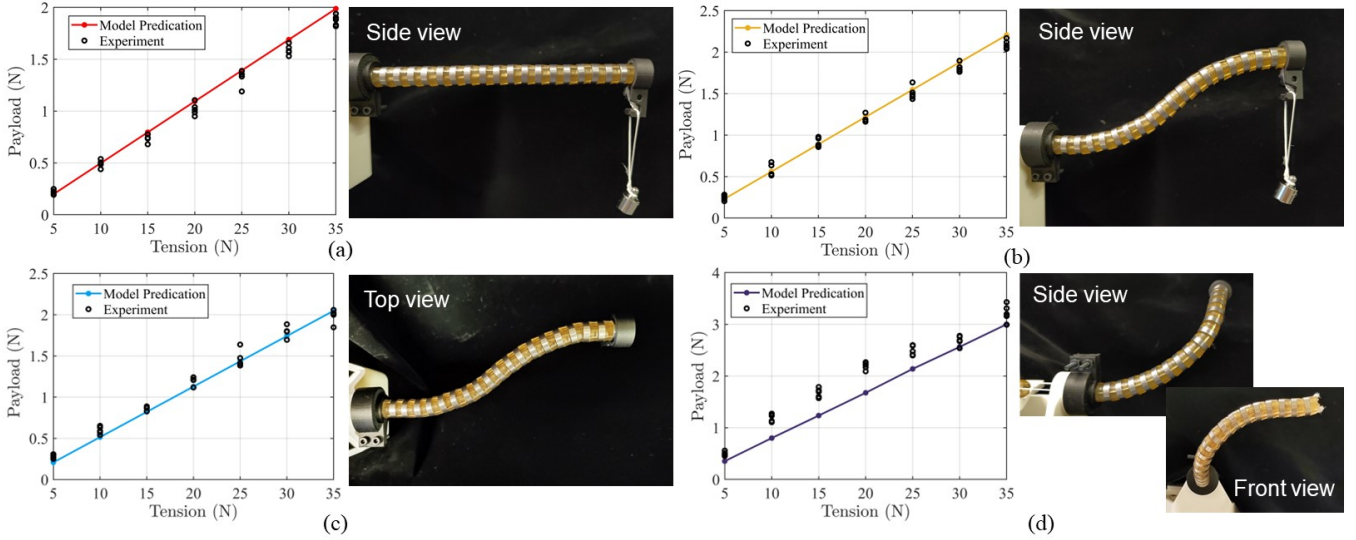


Fig. 6. Experimental validation of our payload capacity model for HARP for different tendon loads (with five experiments for each tendon load) and four different snake configurations: (a) straight configuration, (b) curved configuration in the horizontal plane, (c) curved configuration in the vertical plane, (d) non-planar spatial configuration.

the straight and vertically curved configurations, respectively. Our model had a mean error of 0.08 N (4.21%) and 0.07 N (3.98%) for the payload prediction of these two configurations, respectively. The maximum errors are 0.15 N (8.44%) and 0.12 N (8.19%), respectively.

The results show that we can in some cases increase the payload capacity by using non-equal tendon tensions, and our model enables the prediction of this increase in the payload capacity. We believe future controllers, together with the model presented herein, can actively adjust the individual actuation tendon tensions to maximize the payload, and in some configurations use reduced actuation tendon tensions while still having a large payload capacity to reduce the stress and fatigue on the actuation tendons.

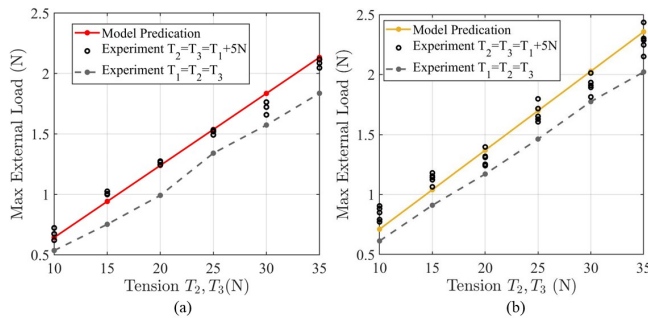


Fig. 7. Experimental validation of the payload capacity of HARP under non-equal tensions, where $T_2 = T_3 = T_1 + 5$ N. (a) Straight configuration. (b) Vertically curved configuration.

Potential sources of error in the experimental validation include small clearance between the 3D printed fixtures and the probe, small deflections in the 3D printed base structure where the snake was mounted, as well as unmodeled tendon elasticity and friction between the actuation tendon and the snake's working channels.

V. CONCLUSIONS

In this paper, we have presented and experimentally validated a statics model for the HARP robot that predicts the robot's payload capacity for any robot shape and actuation tendon loads. We experimentally validated the model for four different robot shapes and two examples where the payload is increased when reducing the force on one actuation tendon. We believe our model will be useful for deriving future actuation controllers to maximize the payload capacity by servoing the actuation tendon forces. Additionally, future motion planners can use this model to plan shapes that maximize the payload capacity.

The main limitation of this work is the computation cost of the solver, which is related to the need to use multiple starts to find a solution and the need to solve the minimization problem for every link in the snake. We believe code optimizations of our implementation can significantly improve the computation time. Analytical spherical joint models in the literature (despite not being directly suitable for determining the payload of our robot) could also be used to provide reasonable initial guesses to the solver and potentially remove the need for multiple starts.

Future work will include extension of this model to include the effects of the inner snake as well as control and planning strategies that utilize this model to optimize the payload through adjusting the probe shape and/or actuation tendon forces.

REFERENCES

- [1] B. Zhao, L. Zeng, Z. Wu, and K. Xu, "A continuum manipulator for continuously variable stiffness and its stiffness control formulation," *Mechanism and Machine Theory*, vol. 149, p. 103746, 2020.
- [2] J. M. You, H. Kim, J. Kim, and D.-S. Kwon, "Design and analysis of high-stiffness hyperredundant manipulator with sigma-shaped wire path and rolling joints," *IEEE Robotics and Automation Letters*, vol. 6, no. 4, pp. 7357–7364, 2021.

- [3] T. Ota, A. Degani, D. Schwartzman, B. Zubiate, J. McGarvey, H. Choset, and M. A. Zenati, "A novel highly articulated robotic surgical system for epicardial ablation," in *2008 30th Annual International Conference of the IEEE Engineering in Medicine and Biology Society*. IEEE, 2008, pp. 250–253.
- [4] A. Degani, H. Choset, A. Wolf, and M. A. Zenati, "Highly articulated robotic probe for minimally invasive surgery," in *Proceedings 2006 IEEE International Conference on Robotics and Automation, 2006. ICRA 2006*. IEEE, 2006, pp. 4167–4172.
- [5] J. Burgner-Kahrs, D. C. Rucker, and H. Choset, "Continuum robots for medical applications: A survey," *IEEE Transactions on Robotics*, vol. 31, no. 6, pp. 1261–1280, 2015.
- [6] A. Orekhov, C. Abah, and N. Simaan, "Snake-like robots for minimally invasive, single-port, and intraluminal surgeries," *The Encyclopedia of Medical Robotics*. World Scientific, pp. 203–243, 2018.
- [7] P. Dupont, N. Simaan, H. Choset, and C. Rucker, "Continuum robots for medical interventions," *Proceedings of the IEEE*, 2022.
- [8] Da Vinci Surgical System, Instrument and Accessory Catalog. Accessed Sept. 9, 2022. [Online]. Available: http://www.unthsc.edu/patientcare/wp-content/uploads/sites/27/Intuitive_Surgical_ins_cat_1_.pdf
- [9] Y.-J. Kim, S. Cheng, S. Kim, and K. Iagnemma, "A novel layer jamming mechanism with tunable stiffness capability for minimally invasive surgery," *IEEE Transactions on Robotics*, vol. 29, no. 4, pp. 1031–1042, 2013.
- [10] P. Berthet-Rayne, G. Gras, K. Leibrandt, P. Wisanuvej, A. Schmitz, C. A. Seneci, and G.-Z. Yang, "The i2Snake robotic platform for endoscopic surgery," *Annals of biomedical engineering*, vol. 46, no. 10, pp. 1663–1675, 2018.
- [11] Y.-J. Kim, S. Cheng, S. Kim, and K. Iagnemma, "A stiffness-adjustable hyperredundant manipulator using a variable neutral-line mechanism for minimally invasive surgery," *IEEE transactions on robotics*, vol. 30, no. 2, pp. 382–395, 2013.
- [12] M. Hwang and D.-S. Kwon, "Strong continuum manipulator for flexible endoscopic surgery," *IEEE/ASME Transactions on Mechatronics*, vol. 24, no. 5, pp. 2193–2203, 2019.
- [13] J. Kim, S.-i. Kwon, Y. Moon, and K. Kim, "Cable-movable rolling joint to expand workspace under high external load in a hyper-redundant manipulator," *IEEE/ASME Transactions on Mechatronics*, vol. 27, no. 1, pp. 501–512, 2021.
- [14] P. Rao, Q. Peyron, S. Lilge, and J. Burgner-Kahrs, "How to model tendon-driven continuum robots and benchmark modelling performance," *Frontiers in Robotics and AI*, vol. 7, p. 630245, 2021.
- [15] M. M. Dalvand, S. Nahavandi, and R. D. Howe, "An analytical loading model for n -tendon continuum robots," *IEEE Transactions on Robotics*, vol. 34, no. 5, pp. 1215–1225, 2018.
- [16] K. Oliver-Butler, J. Till, and C. Rucker, "Continuum robot stiffness under external loads and prescribed tendon displacements," *IEEE Transactions on Robotics*, vol. 35, no. 2, pp. 403–419, 2019.
- [17] P. M. Loschak, S. F. Burke, E. Zumbro, A. R. Forelli, and R. D. Howe, "A robotic system for actively stiffening flexible manipulators," in *2015 IEEE/RSJ International Conference on Intelligent Robots and Systems (IROS)*. IEEE, 2015, pp. 216–221.
- [18] S. Tully, G. Kantor, M. A. Zenati, and H. Choset, "Shape estimation for image-guided surgery with a highly articulated snake robot," in *2011 IEEE/RSJ International Conference on Intelligent Robots and Systems*. IEEE, 2011, pp. 1353–1358.
- [19] A. Faraz and S. Payandeh, "Towards approximate models of coulomb frictional moments in:(i) revolute pin joints and (ii) spherical-socket ball joints," *Journal of engineering mathematics*, vol. 40, no. 3, pp. 283–296, 2001.
- [20] L. Gutkowski and G. Kinzel, "A Coulomb friction model for spherical joints," in *International Design Engineering Technical Conferences and Computers and Information in Engineering Conference*, vol. 9396. American Society of Mechanical Engineers, 1992, pp. 243–250.